

Deep H-band Galaxy Counts and Half-light Radii from HST/NICMOS Parallel Observations

Lin Yan¹

Patrick J. McCarthy¹, Lisa J. Storrie-Lombardi¹, & Ray J. Weymann¹

ABSTRACT

We present deep galaxy counts and half-light radii from F160W ($\lambda_c = 1.6\mu$) images obtained with NICMOS on HST. Nearly 9 arcmin² have been imaged with camera 3, with 3σ depths ranging from $H = 24.3$ to 25.5 in a $0.6''$ diameter aperture. The slope of the counts fainter than $H = 20$ is 0.31, and the integrated surface density to $H \leq 24.75$ is 4×10^5 galaxies per square degree. The half-light radii of the galaxies declines steeply with apparent magnitude. At $H = 24$ we are limited by both the delivered FWHM and the detection threshold of the images.

Subject headings: galaxies: evolution - cosmology: observations - infrared: galaxies.

Accepted for publication in ApJ Letters

¹The Observatories of the Carnegie Institution of Washington,
813 Santa Barbara St., Pasadena, CA 91101

1. Introduction

Galaxy counts as a function of apparent magnitude probe both the geometry of the Universe and the dynamical and luminosity evolution of galaxies. Evolutionary effects dominate the departures of the counts from the Euclidean expectation. The relative importance of the two primary forms of evolution, density and luminosity evolution, can only be properly assessed with spectroscopic redshifts. The near-IR pass-bands, however, are better suited than visible colors to purely photometric surveys as they are less sensitive to star formation and extinction. The weak dependence of the k-correction on Hubble type (Poggianti 1997) and its slow change with redshift further enhance the value of observing at wavelengths beyond $\sim 1\mu\text{m}$.

The deepest visible galaxy counts yield an integrated galaxy number density of $2 \times 10^6 / \text{degree}^2$ to $m(\text{F814W}) = 29$ (Williams et al. 1996). The deepest K-band counts reach $K = 23.5$ with limited areal coverage ($\sim 2 \text{ arcmin}^2$) and have a slope of $d \log N/dm \sim 0.2 - 0.3$ for $K > 18$ (Gardner, Cowie, & Wainscoat 1993; Djorgovski et al. 1995; Moustakas et al. 1997). The Near Infrared Camera and Multi-Object Spectrograph (NICMOS; Thompson et al. 1998) on HST offers a means to extend the existing near-IR galaxy counts to much fainter levels in the equivalent of the H and J pass-bands. Parallel observations, in particular, provide modest sky coverage for deep galaxy counts. At the depth of the deepest Keck/NIRC K (2.2μ) counts our areal coverage is presently $\sim 9 \text{ arcmin}^2$ and will increase as subsequent parallel exposures are taken. Our deepest pointings presently cover an area comparable to the deepest NIRC images, but are roughly one magnitude deeper.

This letter, and the independent work of Teplitz et al. (1998), present the first deep H-band galaxy counts with NICMOS. Our data reach $H \sim 24.8$ (50% completeness limit), deeper than all previous published near infrared counts. The F110W ($\sim J$) data, future parallel imaging observations and a more detailed treatment of the present data will be presented in a separate publication.

2. Observations and Data Reduction

The data were obtained with camera 3 of NICMOS operating in the parallel mode, beginning in November 1997. The NICMOS internal pupil adjustment

mirror was set near the end of its range, providing the best possible focus for camera 3. The PSF, measured from the stars in a selected globular cluster field, is slightly non-gaussian, but is well characterized by $\text{FWHM} = 0.25''$.

We obtained four images per orbit, two each with the F110W ($\lambda_c = 1.1\mu$) and F160W ($\lambda_c = 1.6\mu$) filters. The field offset mirror (FOM) was used to dither between two fixed positions $1.8''$ apart in a direction aligned with one axis of the detector. In addition there were small inter-orbit dither moves executed for some of the pointings. The detector was read using the STEP64 MultiAccum sample sequence, with 13 or 18 samples, resulting in exposure times of 256 and 576 seconds, respectively. The projected size of a camera 3 pixel is $0.204''$, giving a $52.2'' \times 52.2''$ field of view for each image. A small area is lost in the construction of the final mosaic image. We selected 12 fields with intermediate to high galactic latitudes for this study (see Table 1). The areal coverage of the present dataset is 8.7 arcmin^2 .

We used McLeod's (1998) NicRed v1.5 package to linearize and remove the cosmic rays from the MultiAccum images. Median images were derived from the 24 pointings and these were used to remove the dark and sky signals. Even with the optimal dark subtraction, there remain considerable frame-to-frame variations in the quality of the final images. We did not estimate photometric error for each individual galaxy due to the frame-to-frame variation, however, as described below, our incompleteness simulation has taken into account this effect for the galaxy number counts. The individual linearized, dark corrected, flatfielded and cosmic ray cleaned images were shifted, masked and combined to produce final mosaic images. Before shifting, each image was 2×2 block-replicated and only integer ($0.1''$) offsets were applied. In this way we avoided any smoothing or interpolation of the data. The MultiAccum process is not 100% efficient in rejecting cosmic ray events and so we applied a 3σ rejection when assembling the final mosaics.

2.1. Galaxy Detection & Photometry

We performed the object detection and photometry using SExtractor version 1.2b10b (Bertin & Arnouts 1996) and photometric zero points provided by M. Rieke (priv. comm) with an uncertainty of 0.05 mag. Each image was convolved with a gaussian kernel with $\text{FWHM} = 0.3''$ for object detection, using a 2.0σ detection threshold. Isophotal magnitudes were mea-

sured to the 1σ isophot.

We define the total magnitude in a manner similar to those used by Smail et al. (1995) and Djorgovski et al. (1995). SExtractor calculates isophotal and aperture magnitudes for each galaxy, along with the isophotal area at a given threshold. We adopted an aperture diameter of $0.6''$. For galaxies with isophotal diameters less than the $0.6''$, we use their aperture magnitudes, after correction to a $2''$ diameter aperture. In using the aperture magnitude as a total magnitude, we assumed that all faint galaxies have similar profiles. We derived the aperture correction from an average of 20 galaxies with isophotal diameters smaller than $0.6''$. This average faint galaxy yielded an aperture correction of 0.3 ± 0.05 magnitudes, indistinguishable from that derived from stars with $H \sim 18$.

For galaxies with isophotal diameters between $0.6''$ and $2''$, we measure isophotal magnitudes to 1σ of sky and then correct to a $2''$ diameter aperture using a correction that is a function of the isophotal magnitude. In our deepest field, for $H < 22.5$, the magnitude correction is negligible, for $22.5 < H < 23.5$ and $H > 23.5$, the corrections are 0.1 and 0.2 mags, respectively. These corrections are derived for each field in the same fashion as the aperture correction described above. Using the galactic foreground extinction A_B derived from the Burstein & Heiles maps (Burstein & Heiles 1984) and the extinction law derived by Rieke & Lebofsky (1985), we find that the maximum extinction correction for our fields is $A_H \sim 0.03$ magnitudes. The new dust maps by Schlegel, Finkbeiner & Davis (1997) gives the maximum A_H of 0.05 mag. Thus, we did not apply any extinction correction to our photometry.

The sky variances, measured in 10 blank $2.5'' \times 2.5''$ areas in each image, give 1σ surface brightness limits ranging from 24.8 to 26.0 mag/arcsec². This implies 3σ limits within a $0.3''$ radius aperture of 24.3 to 25.5 magnitudes.

2.2. Incompleteness Modeling

The raw counts must be corrected for false detections and incompleteness due to crowding, flat-field and dark correction errors, and Poisson noise before meaningful conclusions can be drawn. We have carried out an extensive series of simulations to quantify the incompleteness effects. We selected several well detected galaxies from an image, dimmed them

by various factors, and added these images into the original image at *random locations*. We then apply the same detection and photometry measuring algorithms as in the original analyses. The use of random positions in the simulation allows us to include completeness corrections arising from non-detections and magnitude errors caused by crowding and spatially dependent errors in the sky subtraction and flat field correction. With this approach we create a matrix, P_{ir} , which is the probability of finding a galaxy with the input magnitude of m_i and the recovered magnitude m_r . The number of input galaxies N_i at each magnitude m_i was chosen to reproduce an initial guess for the slope of the counts. The number of galaxies recovered at magnitude m_i , N_r , is obtained from $\sum_i P_{ir} \times N_i$. The detection rate r_i is N_r/N_i , and the completeness correction at the corresponding magnitude bin is $1/r_i$. For each image, we did more than 10^4 simulations to estimate the incompleteness corrections. We performed the incompleteness modeling for four fields with representative integration times. The correction was applied to the individual fields before the final galaxy number counts were produced.

Of our 12 fields, 3 are at intermediate galactic latitudes. In these fields we identified stars using the SExtractor star/galaxy classifier. We found 4 stars with magnitudes $20 < H < 22$, which implies an average 2% correction to the number counts; for $H > 22.0$, the correction at each magnitude bin is $< 2\%$. At $H > 24$, the counts are dominated by compact galaxies in all of our fields. In addition, the measurements of half-light radii vs. total magnitude suggest that the stellar contamination in all of our fields is of the order of few percent.

We estimated our false positive detection rate by reducing the “left” and “right” dither positions independently and by splitting our longest pointing into three independent, but shallower, data sets. The “left” and “right” dither position images allowed us to assess the impact of persistent cosmic rays, while the photometric catalogs in the 1/3 exposure time images of 1120+1300 allowed us to assess the number of detections that had no corresponding object in the deeper image. Both approaches yield false detection rates in the a few percent range in the faintest magnitude bin for each field.

2.3. Half-light Radii

We measured the half-light radius for each object in the final photometric catalog. A subsection of the

image centered on each object was extracted and re-gridded with $20\times$ finer sampling. The enclosed flux was then computed in $0.005''$ steps ($1/20$ pixel) until one half of the total flux was enclosed. The code used for this operation was kindly provided by I. Smail and so our results can be directly compared to Smail et al. (1995). We measured the half-light radius of stars with $16 < H < 23$ in one globular cluster field to derive the instrumental half-light radius. The non-gaussian shape of the PSF requires this measurement to allow comparison with the derived galaxy sizes.

2.4. Results and Discussion

Our deepest field, 1120+1300, is shown in Figure 1 (Plate []). We have circled several representative faint galaxies and noted their magnitudes. The two brightest galaxies in this field have isophotal magnitudes of 17.6 and 18.8, respectively. In Figure 2, we plot the raw and corrected differential galaxy number counts. Table 2 lists the raw counts, incompleteness corrected counts and effective area at each magnitude bin. We determine a slope of 0.31 ± 0.02 for $20 < H < 24.5$, consistent with values derived at K by various groups (Gardner et al. 1993; Djorgovski et al. 1995; Moustakas et al. 1997). We find no significant change in the slope for $H < 24.5$. In the same figure, we plot the counts measured in I and K passbands by Smail et al. (1995), Williams et al. (1996), and Djorgovski et al. (1995). The integrated number of galaxies $H \leq 24.5$, including the incompleteness corrections, is 4×10^5 per sq. degree, or 2×10^{10} galaxies over the entire sky. This is about 3 times larger than the total implied from integration of the local luminosity function (Lin et al. 1996) to $0.01L^*$ over an all-sky co-moving volume for $(\Omega_0, \Omega_\Lambda) = (1, 0)$ cosmological model.

The unambiguous interpretation of the measured counts-magnitude relation in the context of the galaxy formation and evolution requires both knowledge of the redshift distribution and the faint-end slope of the luminosity function. Our images probe the faint-end slope as well as the distant universe. At $z=1$ $H=24$ corresponds to a luminosity of $\sim 0.01L^*$, ($H_0 = 50 \text{ kms}^{-1} \text{ Mpc}^{-1}$, $q_0 = 0.1$, $M_K^* = -24.75$ (Gardner et al. 1997; Glazebrook et al. 1995)). The K-band selected spectroscopic surveys of Cowie et al. (1996; 1997) reach a median z of unity at $K=20-21.5$, equivalent to $H \sim 21-22.5$ for mild to passively evolving populations at $z \sim 1$. Thus our deep counts must contain a large number of $z > 1$ galaxies. The Lyman break selected

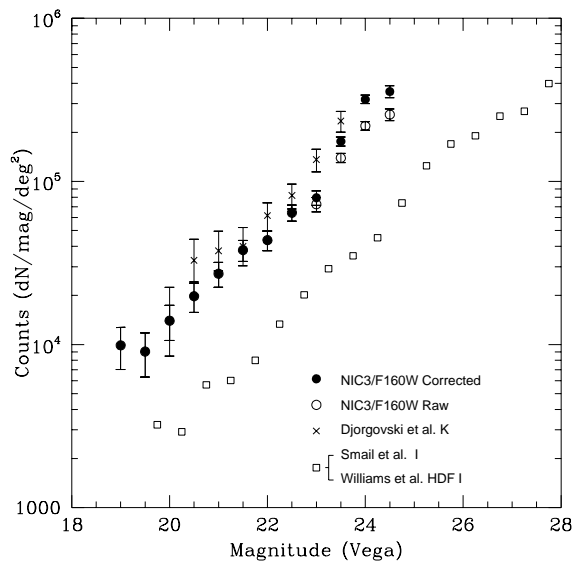


Fig. 2.— The galaxy number count - magnitude relation derived from our data and other surveys from the literature. The open and filled circles are the raw and corrected NICMOS H counts, respectively. The crosses are Djorgovski et al.'s K (2.2μ) counts, the open squares are the average of the I-band counts from Smail et al. (1995) and Williams et al. (1996), with a zero-point shift of 0.48 magnitudes applied to the AB magnitudes in Williams et al. to bring them to the system used in Smail et al.

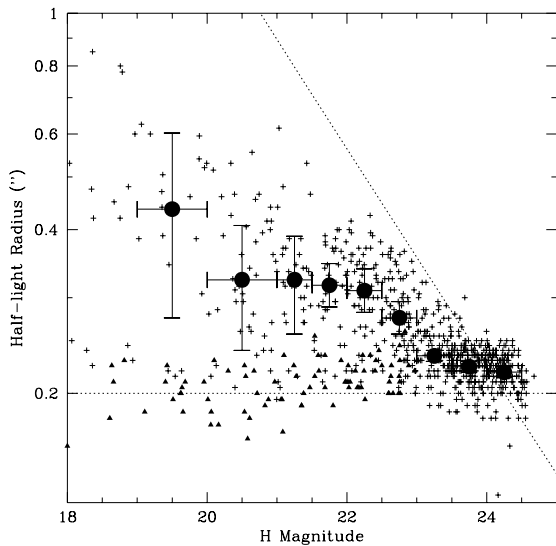


Fig. 3.— The half-light radii for all of the detected galaxies. Stellar objects are indicated by star symbols and galaxies by open circles. The solid dots indicate the median sizes in bins of 0.5 or 1 magnitude widths. At $H = 24$, we have reached the NIC3 angular resolution limit, $0.2''$. The diagonal dotted line shows the magnitude enclosed in an aperture of radius r with a uniform surface brightness of 22 magnitudes/arcsec².

galaxies with spectroscopic redshifts also have K-band magnitudes of $\sim 21.5-23$ (Steidel et al. 1996), within the depths of the counts presented here. What is unclear at present is if the median redshift continues to climb at faint H and K magnitudes or if low luminosity galaxies make an increasing contribution to the counts at $H > 23$. This could be clarified by the photometric redshift measurements of these faint galaxies. The shallow and deep K-band surveys by Huang et al. (1997) and Cowie et al. (1996; 1997) find B–K colors that become increasingly blue for galaxies with $K > 18$, suggesting an increasing contribution from star forming systems. If the bulk of the galaxies that we detect at $H \sim 24$ are faint dwarf galaxies with luminosity much less than L^* at low redshifts instead of L^* galaxies at $z > 3$, the counts slope of 0.31 implies a luminosity function $\Phi(L) \propto L^{-1.78}$, steeper than the local luminosity function. Although there is some evidence that the faint end of the local luminosity function may be steeper than the standard value of -1 (Lilly et al. 1995), a slope of -1.78 has not been observed.

In Figure 3 we plot the measured half-light radii for all of the galaxies in our photometric catalog against their total magnitudes. We computed the median sizes in bins of 0.5 or 1 magnitude widths with the error bars as $\pm 1\sigma$ of the mean and these are shown as the solid symbols in Figure 3. The dotted line corresponds to a uniform surface brightness of 22 mag/arcsec². It is clear from the crowding of points at the faint end into the small area between the stellar locus and the surface brightness limit, that there are strong surface brightness selection effects in our sample at the faint end. Resolved objects with magnitudes fainter than $H \sim 24$ are undetectable in our data. For $H < 22 - 23$, however, there appears to be a real deficit of galaxies near our surface brightness limit, suggesting that the decrease in median half-light radius in the range $20 < H < 23$ is genuine. Images obtained with the high resolution cameras on NICMOS will allow one to extend the study of galaxy scale lengths to scales of $\lesssim 0.1''$, but the surface brightness selection biases will, on average, be more severe for these data.

The NICMOS pure parallel program offers us a wealth of unique data with high angular resolution and unprecedented photometric depth in the H and J bands over an area of ~ 100 arcmin². We will be able to carry out much more detailed studies, such as deep number counts as functions of morphologi-

cal types and colors, the evolution of galaxy intrinsic sizes. Combined with ground-based optical photometry and spectroscopy, we may be able derive photometric redshifts for the numerous faint galaxies detected in the galaxy number counts.

3. Acknowledgements

We thank the staff of the Space Telescope Science Institute for their efforts in making this parallel program possible. In particular we thank Peg Stanley and the staff of the PRESTO division, Bill Sparks, John Mackenty, and Daniella Calzetti of the NICMOS group and Bob Williams and Duccio Macchetto of the director's office. We acknowledge useful discussions with D. Hogg, I. Smail, R. Thompson, & M. Rieke. B. McLeod and I. Smail are thanked for generously allowing the use of their software for the data reduction and scale length measurements. This research was supported, in part, by grants from the Space Telescope Science Institute, GO-7498.01-96A and P423101. This project made use of the NASA/IPAC Extragalactic Database, operated by the Jet Propulsion Laboratory, California Institute of Technology, under contract with the National Aeronautics and Space Administration.

REFERENCES

Bertin, E., & Arnouts, S. 1996, *A&AS*, 117, 393

Cowie, L.L. et al. 1997, in prep.

Cowie, L.L., 1996, *AJ*, 112, 839

Djorgovski, S., Soifer, B.T., Pahre, M.A., Larkin, J.E., Smith, J.D., Neugebauer, G., Smail, I., Matthews, K., Hogg, D.W., Blandford, R.D., Cohen, J., Harrison, W., Nelson, J. 1995, *ApJ*, 438, L13

Gardner, J.P., Cowie, L.L., & Wainscoat, R.J. 1993, *ApJ*, 415, 9

Gardner, J.P., Sharples, R.M., Frenk, C.S., Baugh, C.M., Carrasco, B.E. 1997, *ApJ*, 480, L99

Glazebrook, K, Peacock, J.A, Miller, L., Collins, C.A. 1995, *MNRAS*, 275, 169

Huang, J.S., Cowie, L.L., Gardner, J.P., Hu, E.M., Songaila, A., Wainscoat, R.J. 1997, *ApJ*, 476, 12

Lilly, S.J., Tresse, L., Hammer, F., Le Fevre, O., Crampton, D. 1995, *ApJ*, 455, 108

Lin, H., Kirshner, R.P., Shectman, S.A., Landy, S.D., Oemler, A., Tucker, D.L., Schechter, P.L. 1996, *ApJ*, 464, 60

McLeod, B. 1998, HST Calibration Workshop, in press

Moustakas, L.A., Davis, M., Graham, J.R., Silk, J., Peterson, B., Yoshii, Y. 1997, *ApJ*, 475, 445

Poggianti, B.M. 1997, *A&AS*, 122, 399

Rieke, G. & Lebofsky, M.J. 1985, *ApJ*, 288, 618

Smail, I., Hogg, D.W., Yan, L. & Cohen, J.G. 1995, *ApJ*, 449, L105

Steidel, C.C., Giavalisco, M., Pettini, M., Dickinson, M., Adelberger, K. 1996, *ApJ*, 462, L17

Teplitz, H.I., Gardner, J.P., Heap, S. et al. 1998, in preparation

Thompson, R.I., Rieke, M., Schneider, G., Hines, D. & Corbin, M. 1998, *ApJ*, 492, L95

Williams, R. E., Blacker, B., Dickinson, M., Dixon, W.V., Ferguson, H.C., Fruchter, A.S., Giavalisco, M., Gilliland, R.L., Heyer, I., Katsanis, R., Levay, Z., Lucas, R.A., McElroy, D.B., Petro, L., Postman, M. 1996, *AJ*, 112, 1335

This 2-column preprint was prepared with the AAS L^AT_EX macros v4.0.

Table 1. The Selected Fields

Field	RA (J2000)	DEC	l (deg)	b (deg)	T(F160W) (sec)	$\mu(1\sigma)$ mag/ \square''	m_{lim} 50%	N_{lim} 50%
0240-0141	02:40:13	-01:41:27	173	-54	2816	24.8	23.8	62
0304-0015	03:04:38	-00:15:04	178	-48	2560	25.3	23.8	25
0457-0456	04:57:19	-04:56:51	204	-28	4480	25.7	24.3	42
0729+6915	07:29:57	69:15:02	146	29	5120	25.9	24.5	31
0744+3757	07:44:32	37:57:21	182	26	2048	25.1	23.5	49
1039+4144	10:39:37	41:44:54	176	59	5376	25.5	24.5	74
1120+1300	11:20:35	13:00:00	242	65	13824	26.0	24.8	137
1237+6215	12:37:33	62:15:27	126	55	4608	25.7	24.3	47
1604+4318	16:04:55	43:18:56	69	48	3840	25.6	24.0	53
1631+3001	16:31:39	30:01:23	50	42	3584	25.1	24.0	88
2220-2442	22:20:12	-24:42:00	28	-56	5120	25.9	24.5	71
2344-1524	23:44:00	-15:24:50	66	-70	3840	25.4	24.0	60

Table 2. Raw and Corrected Counts

Mag.	$\log N_{\text{raw}}$ deg ⁻² mag ⁻¹	$\log N_{\text{corr}}$ deg ⁻² mag ⁻¹	$-\sigma$	$+\sigma$	A_{eff} arcmin ²
19.0	3.995	3.995	0.148	0.11	8.7
19.5	3.957	3.957	0.156	0.114	8.7
20.0	4.146	4.146	0.121	0.094	8.7
20.5	4.296	4.296	0.099	0.081	8.7
21.0	4.434	4.434	0.083	0.070	8.7
21.5	4.579	4.579	0.069	0.0597	8.7
22.0	4.640	4.640	0.064	0.056	8.7
22.5	4.808	4.808	0.052	0.0466	8.7
23.0	4.860	4.900	0.047	0.042	8.7
23.5	5.144	5.267	0.028	0.028	8.7
24.0	5.340	5.503	0.026	0.026	6.5
24.5	5.410	5.551	0.038	0.035	2.9

Note: Errors are in logarithmic scale and A_{eff} is the effective area at each magnitude bin.

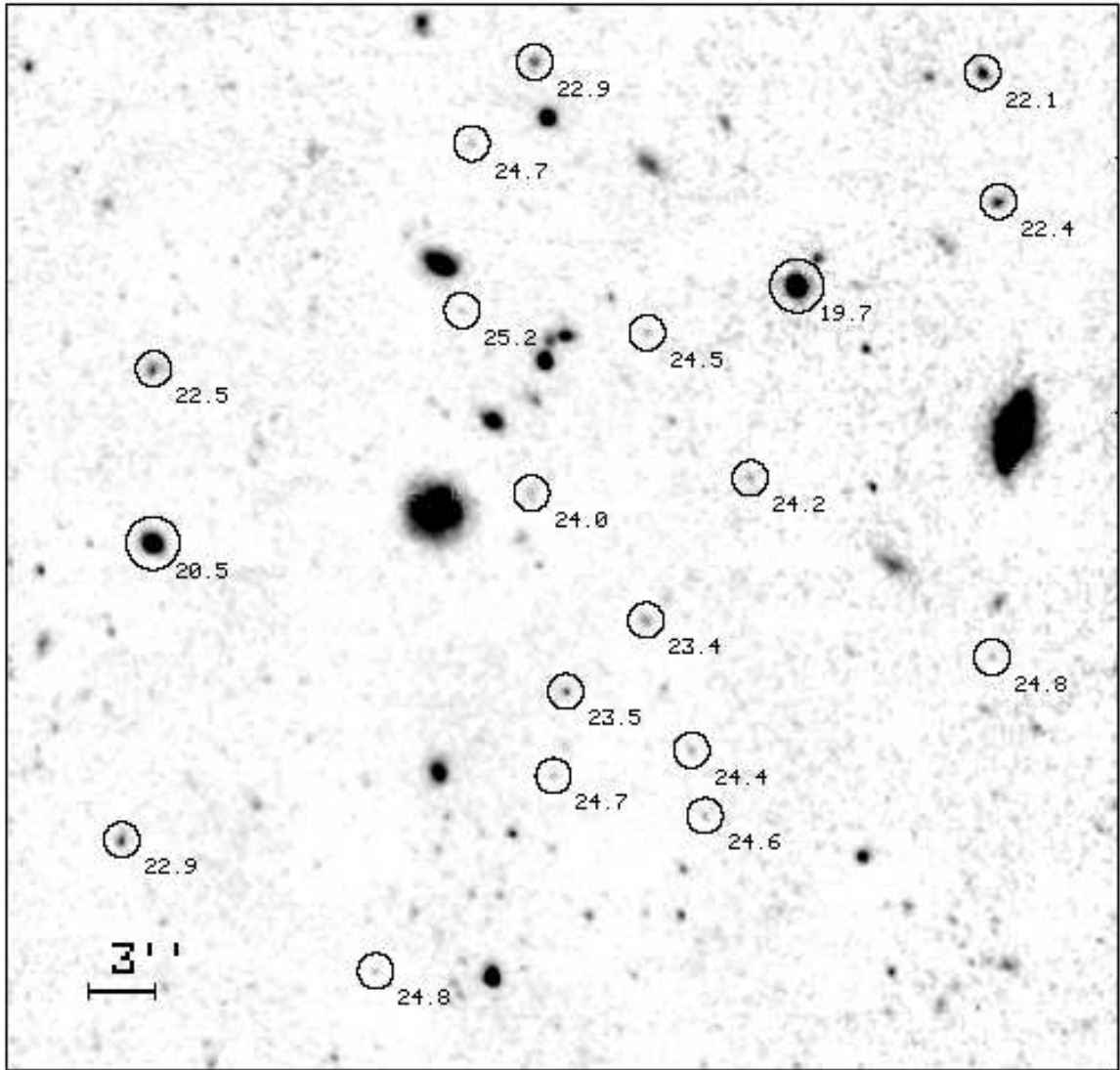


Fig. 1.— A greyscale representation of our deepest field, 1120+1300. Several faint objects are marked and their H magnitudes are noted. The field shown is $50.2'' \times 50.2''$.